

A multi-wavelength study of the oxygen-rich AGB star CIT 3: Bispectrum speckle interferometry and dust-shell modelling

K.-H. Hofmann¹, Y. Balega², T. Blöcker¹, and G. Weigelt¹

¹ Max-Planck-Institut für Radioastronomie, Auf dem Hügel 69, D-53121 Bonn, Germany

(hofmann@mpifr-bonn.mpg.de, bloecker@mpifr-bonn.mpg.de, weigelt@mpifr-bonn.mpg.de)

² Special Astrophysical Observatory, Nizhnij Arkhyz, Zelenchuk region, Karachai-Cherkesia, 35147, Russia (balega@sao.ru)

Received date / accepted date

Abstract. CIT 3 is an oxygen-rich long-period variable evolving along the Asymptotic Giant Branch and is one of the most extreme infrared AGB objects. Due to substantial mass loss it is surrounded by an optically thick dust shell which absorbs almost all visible light radiated by the star and finally re-emits it in the infrared regime. We present the first near infrared bispectrum speckle-interferometry observations of CIT 3 in the J -, H -, and K' -band. The J -, H -, and K' -band resolution is 48 mas, 56 mas, and 73 mas, resp. The interferograms were obtained with the Russian 6 m telescope at the Special Astrophysical Observatory. While CIT 3 appears almost spherically symmetric in the H - and K' -band it is clearly elongated in the J -band along a symmetry axis of position angle -28° . Two structures can be identified: a compact elliptical core and a fainter north-western fan-like structure. The eccentricity of the elliptical core, given by the ratio of minor to major axis, is approximately $\varepsilon=123\text{ mas}/154\text{ mas}=0.8$. The full opening angle of the fan amounts to approximately 40° . Extensive radiative transfer calculations have been carried out and confronted with the observations taking into account the spectral energy distribution ranging from $1\ \mu\text{m}$ to $1\ \text{mm}$, our near-infrared visibility functions at $1.24\ \mu\text{m}$, $1.65\ \mu\text{m}$ and $2.12\ \mu\text{m}$, as well as $11\ \mu\text{m}$ ISI interferometry. The best model found to match the observations refers to a cool central star with $T_{\text{eff}} = 2250\ \text{K}$ which is surrounded by an optically thick dust shell with $\tau(0.55\ \mu\text{m}) = 30$. The models give a central-star diameter of $\Theta_* = 10.9\ \text{mas}$ and an inner dust shell diameter of $\Theta_1 = 71.9\ \text{mas}$ being in line with lunar occultation observations. The inner rim of the dust-shell is located at $r_1 = 6.6R_*$ and has a temperature of $T_1 = 900\ \text{K}$. The grain sizes were found to comply with a grain-size distribution according to Mathis et al. (1977) with $n(a) \sim a^{-3.5}$, and $0.005\ \mu\text{m} \leq a \leq 0.25\ \mu\text{m}$. Uniform outflow models, i.e. density distributions with $\rho \sim 1/r^2$, turned out to underestimate the flux beyond $20\ \mu\text{m}$. A two-component model existing of an inner uniform-outflow shell region ($\rho \sim 1/r^2$) and an outer region where the density declines more shallow as $\rho \sim 1/r^{1.5}$ proved to remove this flux deficiency and to give the best overall match of the observations. The transition between both density distributions is at $r_2 = 20.5r_1 = 135.7R_*$ where the dust-shell temperature has dropped to $T_2 = 163\ \text{K}$. Provided the outflow velocity kept constant, the more shallow density distribution in the outer shell indicates that mass-loss has decreased with time in the past of CIT 3. Adopting $v_{\text{exp}} = 20\ \text{km/s}$, the termination of that mass-loss decrease and the begin of the uniform-outflow phase took place 87 yr ago. The present-day mass-loss rate can be determined to be $\dot{M} = (1.3 - 2.1) \cdot 10^{-5}\ M_\odot/\text{yr}$ for $d = 500 - 800\ \text{pc}$.

Key words. Techniques: image processing — Circumstellar matter — Stars: individual: CIT 3 — Stars: mass-loss — Stars: AGB and post-AGB — Infrared: stars

1. Introduction

Within the framework of the Two Micron Sky Survey or Infrared Catalogue (IRC, Neugebauer & Leighton 1969), Ulrich et al. (1966) published a list of 14 bright (at $2.2\ \mu\text{m}$) and very red objects being of potential interest for the study of cool and dust-enshrouded stars. Among these so-called CIT objects is CIT 3 (= WX Psc = IRC+10 011 = IRAS 01037+1219), an oxygen-rich long-period variable evolving along the Asymptotic Giant Branch (AGB) and one of the most extreme infrared AGB objects.

CIT 3 belongs to the very late-type AGB stars having a spectral type of M9-10 (Dyck et al. 1974, Lockwood 1985). It is very faint in the optical ($V > 20\ \text{mag}$) but bright in the infrared ($K=2\ \text{mag}$). Given this spectral type and the exceptionally large color index of $V - K \gtrsim 18$, its effective temperature can be estimated to be $\simeq 2500\ \text{K}$ or less considering the effective temperature scales of Dyck et al. (1996,1998) and Perrin et al. (1998). CIT 3 is a regular pulsational variable with a mean infrared variability period of 660 days (Harvey et al. 1974, Le Bertre 1993, Whitelock et al. 1994). The stellar surface of CIT 3 is eroded by strong stellar winds with current mass-loss rates close to $10^{-5}\ M_\odot/\text{yr}$. For example, various CO observations indicate rates in the range of 0.79 up to $2.6 \times 10^{-5}\ M_\odot/\text{yr}$,

resp. (Neri et al. 1998, Loup et al. 1993, Knapp & Morris 1982, Sopka et al. 1989, Knapp et al. 1982). Accordingly, CIT 3 is surrounded by a thick dust shell. This dust shell absorbs almost all visible light radiated by the star and finally re-emits it in the infrared regime. The circumstellar envelope of CIT 3 shows SiO (Dickinson et al. 1978, Desmurs et al. 2000), H₂O (Dickinson 1976, Bowers & Hagen 1984) and OH maser emission (Wilson et al. 1970, Olmon et al. 1980). The expansion velocity of the circumstellar shell amounts to 19 km/s if measured in the 1612 MHz OH maser lines (Baud 1981), and 18 km/s to 23 km/s, with a mean value of 21 km/s, if measured in CO(1-0) and CO(2-1) transitions (Loup et al. 1993).

The angular radius of the OH emitting shell region has been determined by Very Large Array (VLA) measurements to be 4''0 (Baud 1981) and 4''4 (Bowers et al. 1983), resp. The corresponding linear OH radius can directly be determined by the so-called phase-lag method utilizing the phase difference between the red-shifted and blue-shifted peak in the 1612 MHz OH spectrum during the regular IR and OH light variations. Due to the difference in light travel time between the emission from the front and the back of the shell, the variations of these two masing regions are out of phase at Earth. Jewell et al. (1980) and van Langevelde et al. (1990) observed a phase lag of 25.5 d and 34 d, resp., resulting in a linear OH shell radius of $R_{\text{OH}} = 3.3 \cdot 10^{14}$ cm and $R_{\text{OH}} = 4.4 \cdot 10^{14}$ cm, resp. Combining the VLA observations with the phase-lag measurements provides an independent method for determining the distance to CIT 3. For instance, Baud (1981) derived $d = 570$ pc using the phase lag of Jewell et al. (1980), the phase lag of van Langevelde et al. (1990) gives $d = 740$ pc. The somewhat larger angular OH radius of Bowers et al. (1983) result in correspondingly smaller distances, i.e. 520 pc and 670 pc. These direct determinations can be compared with other, indirect, methods. For instance, Hyland et al. (1972) give a distance of 510 pc based on the measured flux at maximum light ($1.1 \cdot 10^{-9}$ W m⁻²) and on the assumption that the maximum stellar luminosity amounts to $10^4 L_{\odot}$. Adopting $L = 2 \cdot 10^4 L_{\odot}$, would result into 720 pc. Whitelock et al. (1994) applied period-luminosity relations to obtain the absolute bolometric magnitude which, together with the apparent magnitude, finally leads to $d = 820$ pc. In summary, the distance to CIT 3 appears to be in the narrow range from 500 to 800 pc.

Zappala et al. (1974) measured the size of CIT 3 at 2.2 μm, 10 μm, and 20 μm by means of lunar occultations. They fitted the disappearance curves at 2.2 μm and 10 μm with two-disks fits. At 2.2 μm, they obtained a small component with an angular diameter of 13 mas contributing 65% of the flux and a larger one with a diameter of 65 mas contributing 35% of the flux. The smaller component was interpreted to be the central star whereas the larger one represents the inner region of the dust shell. At 10 μm, the fit yielded one component of approximately 65 mas diameter providing 15% of the flux, and one of 135 mas providing 85% of the flux. In summary, CIT 3 appeared to consist of a central star with a diameter of 13 mas, surrounded by a dust shell with typical diameters of 65 mas at 2.2 μm and 135 mas at 10 μm.

Recent mid-infrared visibility measurements were carried out by Sudol et al. (1999) and Lipman et al. (2000). Sudol et

al. (1999) quote an upper limit of 0''.63 for the 11 μm shell diameter since CIT 3 was not resolved in their 2.3 m telescope images. Interferometric measurements of Lipman et al. (2000) with the Infrared Spatial Interferometer (ISI) clearly resolve the object at 11 μm indicating an inner dust-shell diameter of 66 mas by means of corresponding radiative transfer models.

There are several pieces of evidence that the dust shell of CIT 3 deviates from spherical symmetry. Marengo et al. (1999) reported evidence for an elongation at 8.55 μm based on 1.5 m telescope data. Neri et al. (1998) fitted their CO observations with two-component Gaussian visibility profiles consisting of a circular and an elliptical component. The circular flux-dominant component corresponds to a spherical envelope with a 29''.6 diameter, the elliptical one to an axisymmetric envelope structure with major and minor axis of 9''.8 and 6''.8, resp, and a position angle of -45° (E to N).

Finally, near-infrared polarimetry (Kruszewski & Coyne 1976, McCall & Hough 1980) revealed that CIT 3 is highly polarized in the *I* and *J*-band with polarization degrees of up to 8-9%. The degree of polarization depends also on the phase. In the *H*- and *K'*-band polarization patterns are less dominant (degree of polarization of the order of 1%). The high degree of polarization either indicates an alignment of the dust particles or an asymmetrical dust-shell structure.

In this paper we present the first bispectrum speckle-interferometry observations of CIT 3 at 1.24 μm (*J*-band), 1.65 μm (*H*-band), and 2.12 μm (*K'*-band). In the *K'*- and *H*-band, the reconstructed images are diffraction-limited, the resolution in the *J*-band is 88% of the diffraction limit. The *J*-, *H*-, and *K'*-band resolution amounts to 48 mas, 56 mas, and 73 mas, resp. Radiative transfer calculations have been conducted to model the spectral energy distribution as well as the various visibility functions in the near and mid-infrared. This paper is organized as follows: In Sect. 2 the bispectrum speckle interferometric observations and data reduction are described. Sect. 3 resumes the results from available mid-infrared long-baseline interferometry. Sect. 4 summarizes the available photometry, spectrophotometry and spectroscopy, and in Sect. 5 radiative transfer modelling and its confrontation with the observations is discussed. Finally, a summary and concluding remarks are given in Sect. 6

2. Observations and data reduction

The CIT 3 speckle interferograms were obtained with the Russian 6 m telescope at the Special Astrophysical Observatory on September 19, 22 and 28, 1999. These dates correspond to the phases $\phi = 0.74, 0.75$ and 0.76 of the periodic variability cycle of 660 days (see Sect. 4.1). The speckle interferograms were recorded with our HAWAII speckle camera (HgCdTe array of 512² pixels, sensitivity from 1 to 2.5 μm) through interference filters with center wavelength/bandwidth of 1.24 μm/0.14 μm (*J*-band), 1.65 μm/0.32 μm (*H*-band) and 2.12 μm/0.21 μm (*K'*-band). Speckle interferograms of the unresolved stars HIP 7740 and HIP 6363 were taken for the compensation of the speckle interferometry transfer function. The observational parameters were as follows: *J*-band observation (Sept. 28): exposure time/frame 80 ms, number of frames 1963

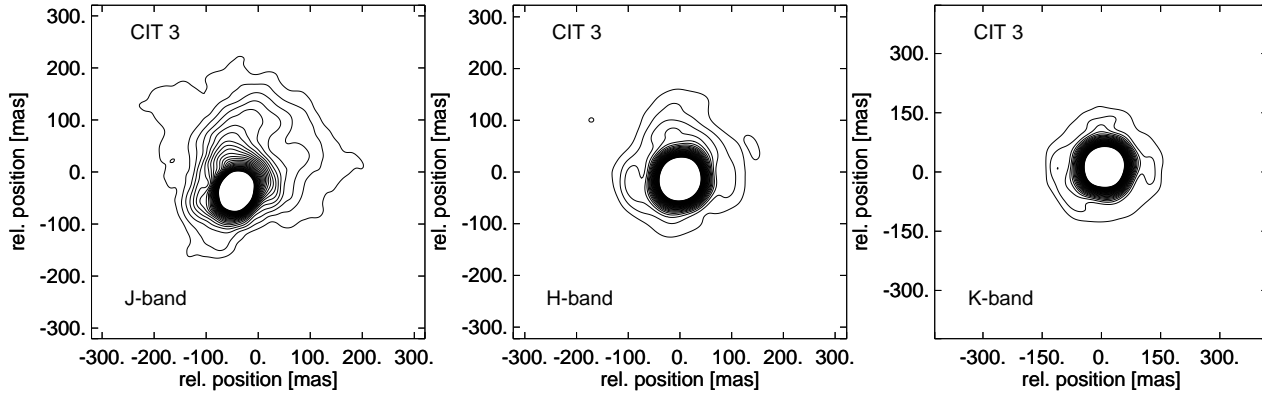


Fig. 1. Contour plots of the reconstructed CIT 3 images at $1.24 \mu\text{m}$ (J -band), $1.65 \mu\text{m}$ (H -band), and $2.12 \mu\text{m}$ (K' -band) from left to right. The J -, H -, and K' -band resolution amounts to 48 mas, 57 mas, and 73 mas, resp. The images in the K' - and H -band are diffraction-limited, the resolution of the J -image is 88% of the diffraction limit. Contour levels are plotted from 1.5% to 29.5% of peak intensity in steps of 1%. North is up and east is to the left.

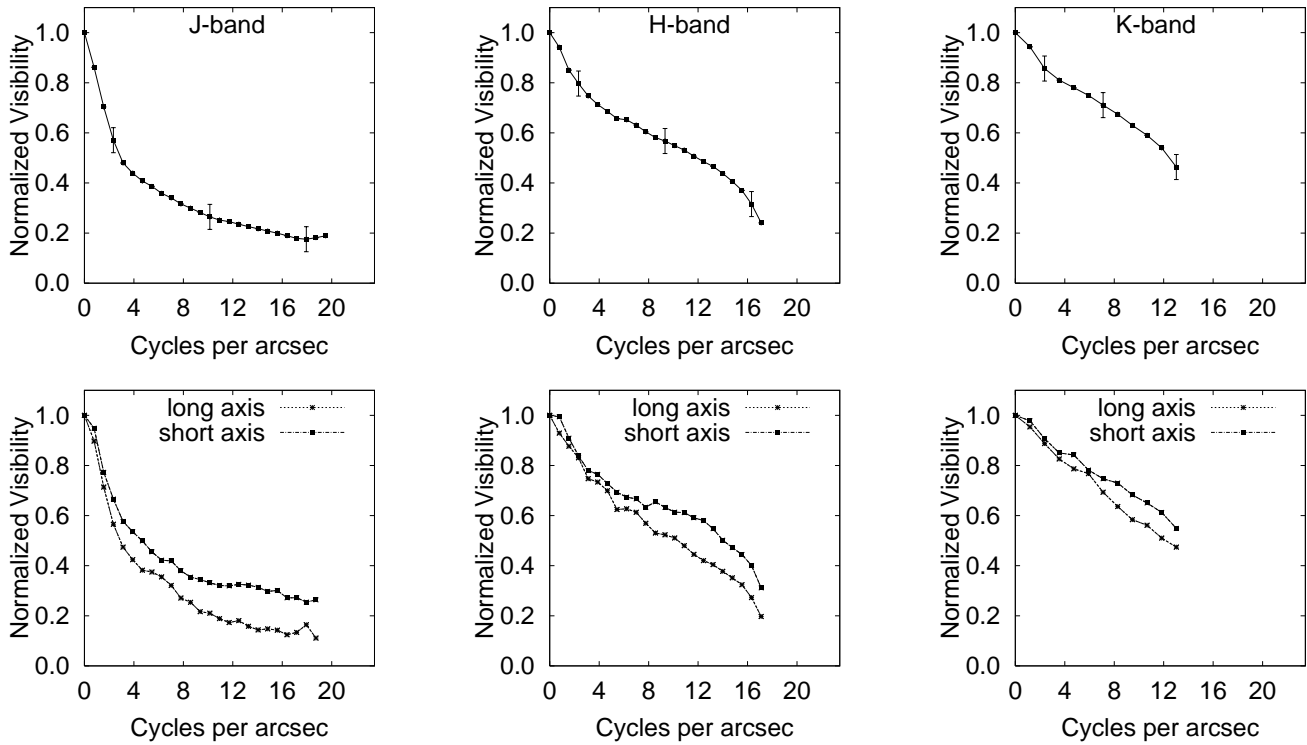


Fig. 2. Visibility functions of CIT 3 at $1.24 \mu\text{m}$ (J -band), $1.65 \mu\text{m}$ (H -band), and $2.12 \mu\text{m}$ (K' -band) from left to right. The top panels show the azimuthally averaged visibilities whereas the bottom panels display visibility cuts at position angles of -28° (long axis) and 62° (short axis), i.e. along and perpendicular to the main symmetry axis of the elongated compact structure of CIT 3 in the J -band (see Fig. 1).

(1268 of CIT 3 and 695 of HIP 6363); H -band observation (Sept. 28): exposure time/frame 20 ms, number of frames 2594 (1723 of CIT 3 and 871 of HIP 6363); K' -band observation (Sept. 19+22): exposure time/frame 25 ms, number of frames 6496 (3016 of CIT 3 and 3480 of HIP 7740); $1.24 \mu\text{m}$ -seeing (FWHM) $\sim 1''.8$; $1.65 \mu\text{m}$ -seeing (FWHM) $\sim 1''.2$; $2.12 \mu\text{m}$ -seeing (FWHM) $\sim 1''.3$; J -band pixel size 13.4 mas, H -band pixel size 20.1 mas, K' -band pixel size 26.4 mas; field of view $3''.4$ (K' -band) and $5''.1$ (H -, J -band). Images of CIT 3 with

48 mas (J -band), 56 mas (H -band), and 73 mas (K' -band) resolution were reconstructed from the speckle interferograms using the bispectrum speckle-interferometry method (Weigelt 1977, Lohmann et al. 1983, Hofmann & Weigelt 1986). The H - and K' -band images are diffraction-limited, the resolution in the J -band is only slightly (12%) below the diffraction limit. The modulus of the object Fourier transform (visibility function) was determined with the speckle interferometry method (Labeyrie 1970).

Figure 1 shows the contour plots of the reconstructed CIT 3 images at $1.24\ \mu\text{m}$, $1.65\ \mu\text{m}$, and $2.12\ \mu\text{m}$. Contour levels are plotted from 1.5% to 29.5% of peak intensity in steps of 1%. The J -band image is clearly elongated along a symmetry axis of position angle -28° . More precisely, two structures can be identified: a compact elliptical core and a fainter north-western fan-like structure. The eccentricity of the elliptical core, given by the ratio of minor to major axis, is approximately $\varepsilon=123\text{ mas}/154\text{ mas}=0.8$. The full opening angle of the fan amounts to approximately 40° , i.e. it extends from position angles -8° to -48° . In the H -band the elongation of the core is hardly visible, and the fan structure is much weaker. Finally in the K' -band, the fan structure has almost disappeared being only present on the 2.5% intensity level, and CIT 3 looks almost spherically symmetric.

Figure 2 displays the corresponding visibility functions of CIT 3 at $1.24\ \mu\text{m}$, $1.65\ \mu\text{m}$, and $2.12\ \mu\text{m}$, i.e. the azimuthally averaged visibilities as well as visibility cuts at position angles of -28° and 62° , i.e. along and perpendicular to the main symmetry axis of the elongated compact structure and the north-western outflow of CIT 3 in the J -band (see Fig. 1). Towards the diffraction limit, the azimuthally averaged visibility functions decline to ~ 0.2 , almost reaching a plateau, at $1.24\ \mu\text{m}$, to ~ 0.25 at $1.65\ \mu\text{m}$ and to ~ 0.45 at $2.12\ \mu\text{m}$. In principle, but most obvious in the J -band, all visibilities show the same behaviour: a sharp decline at low spatial frequencies ($\lesssim 3\text{-}4$ cycles/arcsec) and an extended run of the curve of smaller slope at larger spatial frequencies almost up to the diffraction limit. This indicates the existence of a compact and of an extended dust-shell component.

The visibility cuts along and perpendicular to the main symmetry axis show similar features. Additionally, as expected, the visibility cuts along the symmetry axis decline stronger than those perpendicular to it, evidencing a larger object extension in this direction. The typical differences between the visibility cuts at large spatial frequencies amount up to 0.15 at $1.24\ \mu\text{m}$ and $1.65\ \mu\text{m}$ and $\lesssim 0.1$ at $2.12\ \mu\text{m}$. In the J - and H -band this position angle dependence can be considered as significant, whereas in the K' -band the differences are of the order of the error bar and thus are negligible.

3. Mid-infrared visibility

Mid-infrared visibilities provide additional pieces of spatial information since they are sensitive to the location of the outer, cooler regions of the dust shell governed by thermal dust-emission, whereas near-infrared visibilities are indicative for the inner, hot dust-formation zones and are subject to scattering. The interferometric $11.15\ \mu\text{m}$ observations of Lipman et al. (2000) with the Infrared Spatial Interferometer at baselines of 4m, 9.6m and 16m are shown in Fig. 3. Note, that the data is not coeval but refers to variability phases (see Sect. 4.1) of 0.58-0.66 (4m), 0.71-0.76 (9.6m) and 0.66-0.71 (16m).

4. Spectral energy distribution

4.1. Variability

CIT 3 is a regular variable with a mean infrared period of 660 d. Infrared lightcurves are given in Harvey et al. (1974), Le Bertre (1993), and Whitelock et al. (1994), and radio lightcurves in Herman & Habing (1985). The period appears to be rather stable with time and has not change since the 1970's. It depends slightly on the wavelength, being somewhat shorter at longer wavelengths. For instance, Le Bertre (1993) determined $P = 668, 661$ and 654 d at $\lambda = 1.24\ \mu\text{m}, 2.19\ \mu\text{m},$ and $4.64\ \mu\text{m}$, resp., and Herman & Habing (1985) found $P = 632\text{ d}$ at $\lambda = 18\text{ cm}$. The amplitudes of the brightness variations show, however, a strong wavelength dependence in the near-infrared. Le Bertre (1993) gives $\Delta m = 2.83, 1.79,$ and 1.29 at $1.24\ \mu\text{m}, 2.19\ \mu\text{m},$ and $4.64\ \mu\text{m}$, resp. Then, at longer wavelengths the amplitude seems to stay roughly constant. Harvey found $\Delta m = 1.5$ at $10\ \mu\text{m}$ and Herman & Habing (1985) $\Delta m = 1.2$ at 18 cm .

The spectrum of CIT 3 shows a $9.7\ \mu\text{m}$ silicate feature in partial self-absorption (see Fig. 3). Monnier et al. (1998) presented multi-epoch $8\text{-}13\ \mu\text{m}$ spectrophotometry (1994-1997) covering more than one variability cycle, and showed that the spectral shape of the silicate feature changes during the cycle. The brightness variation between minimum and maximum light was $\sim 1.2\text{ mag}$.

Thus, the variability-phase dependence of the spectral energy distribution (SED) can be characterized by wavelength independent variations of $\Delta m \sim 1.2$ for $\lambda \gtrsim 10\ \mu\text{m}$, a changing spectral shape of the $9.7\ \mu\text{m}$ silicate feature, and significant spectral shape changes for $\lambda \lesssim 5\ \mu\text{m}$ emphasizing the need of coeval data to construct the SED.

All variability phases given in this paper refer to a period of $P = 660\text{ d}$ and to $\phi = 0$ (or 1; maximum light) at JD 2446990 (July 13, 1987) as in Le Bertre (1993).

4.2. Data compilation

To construct the SED various observations are available, as e.g. photometry from the near to the mid-infrared (Ulrich et al. 1966, Wisniewski et al. 1967, Hyland et al. 1972, Morrison & Simon 1973, Dyck et al. 1974, Strecker & Ney 1974, Merrill & Stein 1976, McCarthy et al. 1977, Epcstein et al. 1980, Price & Murdock 1976, Lockwood 1985, Jones et al. 1990, Fouque et al. 1992, Xiong et al. 1994), sub-millimeter (Sopka et al. 1985), millimeter (Walmsley et al. 1991) and radio (e.g. Olmon et al 1980) observations, spectrophotometry and spectroscopy (Lambert et al. 1980, Monnier et al. 1998, Lancon & Wood 2000), as well as photometry and spectroscopy obtained by IRAS (InfraRed Astronomical Satellite; Point Source Catalogue 1985, Volk & Cohen 1989) and ISO (Infrared Space Observatory; Sylvester et al. 1999, Markwick & Millar 2000).

Figure 3 displays those observations either taken close to or being adustable to the pulsational phase ϕ of the present speckle measurements covering a wavelength range from $1\ \mu\text{m}$ to 1.3 mm . This concerns the photometry of Jones et al. (1990) [$\phi = 0.77$], the ISO SWS [$\phi = 0.22$] and LWS [$\phi = 0.49$] spectroscopy of Sylvester et al. (1999), the $400\ \mu\text{m}$ data of Sopka et al. (1985) [$\phi = 0.89$], and the 1.3 mm data of

Walmsley et al. (1991) [$\phi = 0.73$]. Phases were calculated according to Sec. 4.1. Additionally IRAS fluxes (scaled to ISO data) are shown. Since the variability's brightness amplitude is \sim constant at mid-infrared and longer wavelengths, the LWS spectrum taken at minimum light can be adjusted (factor 1.4, see Sylvester et al. 2000) to meet the SWS spectrum. Finally the complete ISO spectroscopy was scaled to match the ground-based photometry of Jones et al. (1990) between $9\mu\text{m}$ and $18\mu\text{m}$. The inlay of Fig. 3 shows the mid-infrared spectrum at $\phi = 0.75$, interpolated from the multi-epoch spectrophotometry of Monnier et al. (1998), as suitable for the present phase of the speckle observations, in comparison with the ISO data. Concerning the silicate feature, absorption is more prominent at minimum light, accordingly the shape of the ISO SWS spectrum (Sylvester et al. 2000) at $\phi = 0.22$ fits better to the minimum than to the maximum light curve.

5. Dust-shell models

To construct models for the dust shell of CIT 3 radiative transfer calculations were carried out using the code DUSTY (Ivezić et al. 1997). The code was expanded for the calculation of synthetic visibilities as described by Gauger et al. (1999). DUSTY solves the radiative transfer problem in spherical symmetry utilizing the self-similarity and scaling behaviour of IR emission from radiatively heated dust (Ivezić & Elitzur 1997). Due to the observed elongation in the J -band the assumption of spherical symmetry appears to be questionable at least on smaller scales. However, on larger scales and for $\lambda > 2.1\mu\text{m}$ the dust shell does not deviate significantly from spherical symmetry and its main properties can be believed to be inferable from such models in fair approximation. Nevertheless, it should be kept in mind that the derived dust-shell properties are subject to the geometry and are, therefore, of tentative character.

The model construction requires the specification of the central radiation source, the dust properties (chemistry, grain sizes), the temperature at the inner dust-shell boundary and the relative thickness of the dust shell (ratio of outer to inner shell radius), the density distribution, and the total optical depth at a given reference wavelength.

The models are confronted with the observed SED and the near- and mid-infrared visibilities. Preference is given to the observations close to the phase of the present speckle observations ($\phi = 0.75$). Concerning the SED, we take into account the ground-based photometry of Jones et al. (1990) [$1.6\mu\text{m}$ - $18\mu\text{m}$], the spectrophotometry of Monnier et al. (1998) [silicate feature], the ISO data of Sylvester et al. (1999) [$5\mu\text{m}$ - $100\mu\text{m}$] scaled to the ground-based photometry, as well as $400\mu\text{m}$ (Sopka et al. 1985) and 1.3mm (Walmsley et al. 1991) data. Interstellar extinction have only minor effects (Alvarez et al. 2000) and was neglected. For instance, Xiong et al. (1994) gives for the interstellar reddening $A_V = 0.18$ mag referring to van Herk (1965).

Previous (spherically symmetric) radiative transfer models were communicated by, e.g., Rowan-Robinson & Harris (1983), Bedijn (1987), Schutte & Tielens (1989), Le Sidaner & Le Bertre (1996), and Lipman et al. (2000). The present radiative transfer models take for the first time a broad range of

the SED (from $1\mu\text{m}$ to 1mm) and visibilities at different wavelengths into account.

5.1. Standard single-shell models

An extensive model grid was calculated for standard uniform-outflow shells, i.e. for density distributions $\sim 1/r^2$ within the dust shell. The central star was approximated by black bodies, however, model atmospheres (Aringer & Loidl, private comm.) were also taken into account. Due to its spectral type of M9-10, CIT 3's effective temperature can be estimated to lie in the range of $\simeq 2500$ - 2700K if extrapolated from the effective temperature scale for giants given by Perrin et al. (1998) (see also Dyck et al. 1998, van Belle et al. 1999). However, long-period variables can be substantially cooler than giants of the same spectral type (van Belle et al. 1999), therefore models were calculated for $T_{\text{eff}} = 2000$ to 3000K . Concerning the optical dust properties we considered different sets of silicate grains (Draine & Lee 1984, Ossenkopf et al. 1992, Le Sidaner & Le Bertre 1993, David & Pegourie 1995). In the following sections we will mostly refer to the Ossenkopf et al. (1992) grains which prove to give good fits to the silicate feature.

For the grain-size distribution we took into account grain-size distributions according to Mathis et al. (1977, hereafter MRN), i.e. $n(a) \sim a^{-3.5}$, with $0.005\mu\text{m} \leq a \leq (0.13 \text{ to } 0.45)\mu\text{m}$ as well as single-sized grains with $a = 0.05$ to $0.3\mu\text{m}$. Grain-size distributions were accounted for by the synthetic grain approximation which first calculates the absorption and scattering efficiencies for each grain and then determines average cross sections by averaging over the size-distribution. The shell thickness was fixed to $Y_{\text{out}} = r_{\text{out}}/r_1 = 10^3$, with r_{out} and r_1 being the outer and inner radius of the shell, respectively. Larger Y_{out} (e.g. 10^4) affect the SED only slightly beyond $100\mu\text{m}$. The model parameters are completed by the dust temperature T_1 at the shell's inner boundary r_1 , which was varied between 400 and 1500K , and the optical depth, τ , at a given reference wavelength, λ_{ref} . Referring to $\lambda_{\text{ref}} = 0.55\mu\text{m}$, optical depths between 10 and 90 were considered.

The inspection of the model grid reveals that a simultaneous match of all observed properties does not appear to be possible within the considered parameter space. In particular, it turned out that uniform outflow models cannot provide enough flux in the far-infrared and simultaneously match the observations at shorter wavelengths. This may indicate higher densities in the outer shell regions than given by the $1/r^2$ density distribution, and thus a more shallow density decline or the existence of regions of enhanced density due to a previous period of increased mass loss (see, e.g., Suh & Jones 1997; Blöcker et al. 1999, 2001). This is in line with the results of Lipman (2000) who found that the ISI visibility data is better fitted by a $1/r^{1.5}$ density fall-off than by a uniform outflow.

The best models found are shown in Fig. 3 and refer to an optical depth of $\tau_V=30$ given by the match of the silicate feature. The grain sizes are strongly constrained by the near-infrared visibilities, and a grain-size distribution appeared to be better suited than single-sized grains. Considering a grain-size distribution, the maximum grain-size was determined to

be $a_{\max} = 0.25 \mu\text{m}$ as in the original MRN distribution. The temperature at the inner rim of the dust shell was found to be in the range of 850-950 K with the best model at 900 K for the best match of visibilities.

The temperature of the central star is not well constrained by the SED or the visibilities. For instance, black bodies of 2000 K and 2500 K yielded similar overall fits given the observational and theoretical uncertainties. However, the lunar occultation observations of Zappala et al. (1974), yielding a central-star diameter of 13 mas and a typical dust-shell diameter of 65 mas at $2.2 \mu\text{m}$, seem to favour lower temperatures if one compares the dimensions of the respective models. For instance, adopting $T_{\text{eff}} = 2000 \text{ K}$ a bolometric flux of $f_{\text{bol}} = 1 \cdot 10^{-9} \text{ W m}^{-2}$ determined by the SED fit gives a central-star diameter of $\Theta_* = 13.7 \text{ mas}$. This leads for $T_1 = 900 \text{ K}$, to an inner dust shell diameter of $\Theta_1 = 65.8 \text{ mas}$ corresponding to $r_1 = 4.8 R_*$ in reasonable agreement with the observations. On the other hand, a star with $T_{\text{eff}} = 2500 \text{ K}$ leads to a smaller central star of $\Theta_* = 8.8 \text{ mas}$ and to a dust shell with $\Theta_1 = 78.2 \text{ mas}$ and $r_1 = 8.9 R_*$. Even though this comparison still lacks corrections due to different pulsational phases, it indicates that CIT 3 should be cooler than, say, 2500 K. Taking into account the model fits and the above constraint, the best suited model is that with $T_{\text{eff}} = 2250 \text{ K}$ giving $\Theta_* = 10.9 \text{ mas}$ and $\Theta_1 = 73.3 \text{ mas}$ ($r_1 = 6.7 R_*$).

The phase dependence of the silicate feature can be seen in the inlay of Fig. 3 showing ground-based photometry and spectrophotometry (Jones et al. 1990, Monnier et al. 1998) and the ISO data (Sylvester et al. 1999). The difference between the spectrophotometry (interpolated for $\phi=0.75$) and the ISO data ($\phi=0.22$) becomes most obvious between $10 \mu\text{m}$ and $13 \mu\text{m}$. Since the scaled ISO data meets the photometry of Jones et al. (1990) ($\phi=0.77$) both at $9 \mu\text{m}$ and $18 \mu\text{m}$, the phase dependence of the spectral shape appeared to be restricted to the above region, at longer wavelengths flux differences are independent of the wavelength. The radiative transfer calculations show that for the considered parameters the spectrophotometry can be matched only in its exact shape on the expense of worsening the fits of other observational quantities as, for instance, the mid-infrared visibility. Additionally, the flux at $18 \mu\text{m}$ cannot be matched and the flux deficit in the far infrared is considerably enlarged.

The near infrared part of the SED tends to require somewhat higher optical depths than, for instance, the silicate feature or the visibilities leading to somewhat higher fluxes than observed. Regarding the observations this may be attributed to the fact that the data is for the same pulsational cycle phase but for different epochs, i.e. to changes of the flux variations during a pulsational cycle over the last decade. With respect to the models, the assumption of spherical symmetry has to be questioned at shorter wavelengths as obvious in the J -band image of Fig. 1. Since the spectra of cool giants can deviate considerably from that of a black body in the optical and near-infrared, we used also model atmospheres (Aringer & Loidl, priv comm., cf. Aringer et al. 1997) instead of simple black bodies for the central source of radiation. The coolest atmosphere used refer to $T_{\text{eff}} = 2700 \text{ K}$ and $\log g = 0$. Due to the high optical depths, the SED fits remained basically unchanged, and the visibil-

ity curves run only somewhat higher than in the corresponding black body calculation. For lower effective temperatures as, e.g., for $T_{\text{eff}} = 2250 \text{ K}$ being appropriate for CIT 3, these differences can be expected to become larger due the increasing strength of molecular absorption bands (e.g. water vapor) which can also be phase dependent (see, e.g., Matsuura et al. 2001). However, due to the lack of model atmospheres in this regime we stayed with the black body approximation.

We note that, while the J - and K' -visibilities decline with almost constant slope at higher spatial frequencies, the H -band visibility shows a significant drop beyond 15 cycles/arcsec. This drop cannot be reproduced by any of the models. Though still not being significant, the development of a similar trend seems to be suggested by the K' -band data close to the diffraction limit. Such a visibility shape can be expected if, for instance, the central star is partially resolved, which, however, requires a stellar diameter of the order of 50 mas and certainly does not apply to CIT 3. The reason for this drop has to remain open yet but may be related to the asphericity of CIT 3.

5.2. Different density distributions

While the above uniform outflow models seem to match the observations reasonably well from the near-infrared to the mid-infrared, they fail to give sufficiently high fluxes beyond, say, $20 \mu\text{m}$. This indicates, for instance, either a flatter density distribution than $\rho \sim 1/r^2$ as given by the standard uniform outflow model or the existence of regions with increased density in the outer shell due to periods of higher mass-loss in the past. We recalculated the main body of the grid with density distributions ranging from $\rho \sim 1/r^2$ to $\rho \sim 1/r^{1.5}$ and combinations of it. It turned out that distributions being generally more shallow can match the silicate feature and the mid-infrared visibility but fail to fit the near-infrared visibilities. Therefore, two-component shells were considered with an inner uniform-outflow component and an outer component with a flatter distribution, i.e. with $\rho \sim 1/r^x$ and $x < 2$. The transition between both density distributions is at the relative radius $Y_2 = r_2/r_1$. Models were calculated for $Y_2 = 2.5$ to 30.5.

We also calculated some uniform outflow models with density enhancements or superwind components, i.e. with regions in the shell where $\rho \sim A \cdot 1/r^2$ with superwind amplitudes A ranging from 10 to 100. However, the spectral index of the far-infrared tail of the SED and the visibilities seem to favour the above flat density distribution in the outer shell region rather than a superwind component.

In order to preserve the match of SED and visibilities up to the mid-infrared the transition to the flatter density distribution should take place in sufficient distance from the inner rim of the dust shell. On the other hand, in order to provide sufficiently high fluxes in the far-infrared the exponent in the density distribution has to be sufficiently small. The best models found are those with $\rho \sim 1/r^2$ for $Y_2 \leq 20.5$ and $\rho \sim 1/r^{1.5}$ for $Y_2 > 20.5$. The temperature T_1 at the inner rim of the dust shell ranges again between 850 and 950 K. Model fits are shown in Fig. 3. Since the transition radius $Y_2 = 20.5$ corresponds to a temperature of $T_2 = 163 \text{ K}$, mostly the outer cool regions

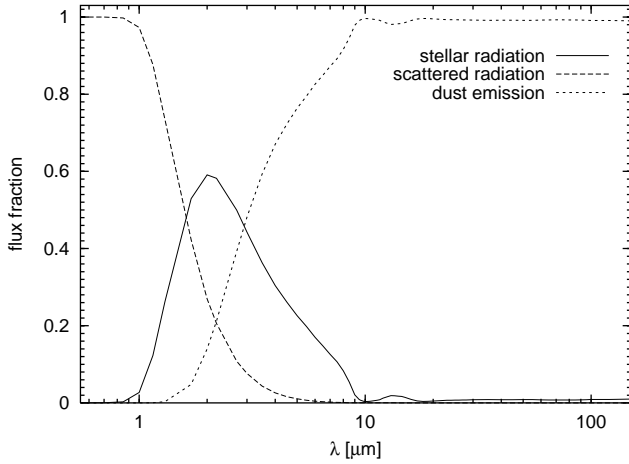


Fig. 4. Fractional contributions of the emerging stellar radiation, the scattered radiation, and of the dust emission to the total flux as a function of the wavelength for a two-component model. The density decreases $\sim 1/r^2$ for $Y_2 \leq 20.5$, and $\sim 1/r^{1.5}$ for $Y_2 > 20.5$. (see Fig. 3). Model parameters are: black body, $T_{\text{eff}} = 2250$ K, $T_1 = 900$ K, $\tau_{0.55\mu\text{m}} = 30$, Ossenkopf et al. (1992) silicates, and a Mathis et al. (1977) grain size distribution with $a_{\text{max}} = 0.25 \mu\text{m}$.

of the dust shell are concerned and the spatial dimension of the dust shell changed only slightly. For $T_{\text{eff}} = 2250$ K and $T_1 = 900$ K, the inner rim of the dust shell is at r_1/R_* = 6.62 corresponding to an angular diameter of $\Theta_1 = 71.9$ mas.

These results can be compared with the radiative transfer model of Lipman et al. (2000). Based on fits of the ISI $11 \mu\text{m}$ visibility data (and the silicate feature) they also found a $1/r^{1.5}$ density fall-off to be better suited to match the observations. However, an overall $1/r^{1.5}$ density law appears to be in conflict with the present near-infrared visibilities leading to too high densities in the inner parts of the shell. The present modelling suggests, as mentioned above, the presence of a sufficiently broad uniform outflow area in the inner shell region before the flatter density distribution takes over.

Fig. 4 shows the fractional contributions of the emerging stellar radiation, the scattered radiation, and of the dust emission to the total flux as a function of the wavelength for the above two-component model. Whereas the radiation at $11 \mu\text{m}$ is almost completely given by thermal dust emission, the radiation in the near-infrared domain is strongly determined by scattering. The contribution of scattered light amounts to 20.6%, 42.3% and 79.2% in the K' -, H - and J -band, resp., while thermal dust emission accounts for 21.2%, 4.8% and 0.2%, resp., and the emerging direct stellar light to 58.2%, 52.9%, and 20.6% resp. It demonstrates that for the given grain-size distribution 49.3%, 89.8% and 99.7% of the dust-shell emission is due to scattering. We note that these derived attributes of the near-infrared emission are subject to some uncertainties due to their dependence on the dust properties and the assumption of spherical symmetry. For instance, though the grain-sizes are strongly constrained by the near-infrared visibilities, principal ambiguities remain due to, e.g., the used optical dust con-

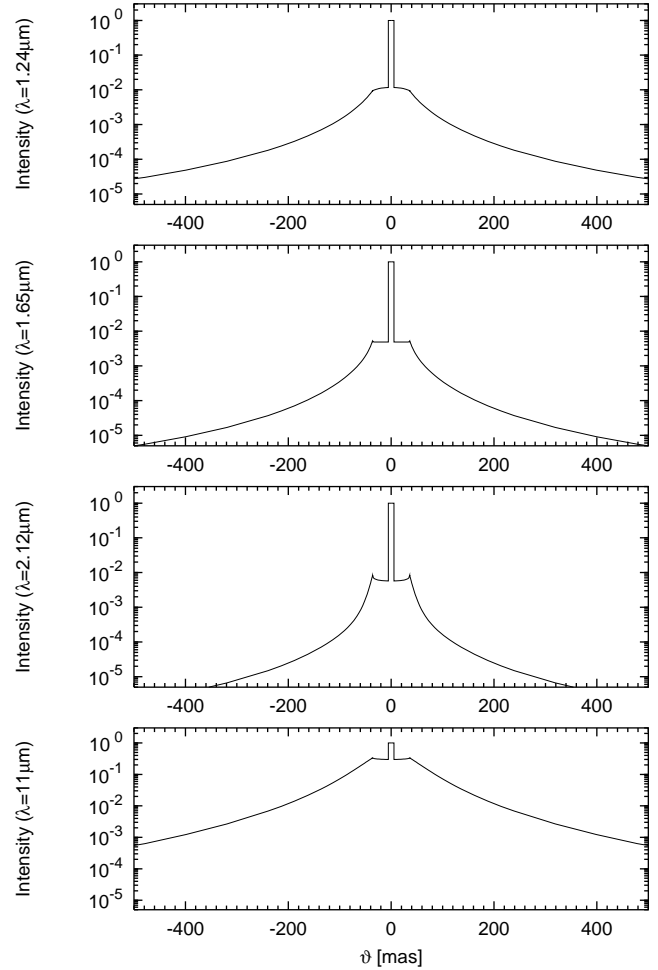


Fig. 5. Normalized intensity at $1.24 \mu\text{m}$, $1.65 \mu\text{m}$, $2.12 \mu\text{m}$, and $11 \mu\text{m}$ (from top to bottom) vs. angular displacement ϑ for a two component model with a uniform outflow in the inner dust shell region and $\rho \sim 1/r^{1.5}$ for $Y_2 > 20.5$ (see Figs. 3-4). The central peak belongs to the central star with a radius of 5.5 mas. The inner hot rim of the circumstellar shell has a radius of 35.9 mas, the cool far-out component with the flatter density distribution is located at a radius of 737 mas beyond the scale of this figure. In the K' -band the inner rim of the circumstellar shell is noticeable limb-brightened. The model refer to $T_{\text{eff}} = 2250$ K, $T_1 = 900$ K, and $\tau(0.55\mu\text{m}) = 30$. The calculations are based on a black body, Ossenkopf et al. (1992) silicates, and a Mathis et al. (1977) grain size distribution with $a_{\text{max}} = 0.25 \mu\text{m}$.

stants depending on shape and chemistry of the grains. Since the resolution of the present speckle observations is of the order of the inner dust-shell boundary, future near-infrared interferometric measurements of higher resolution can yield further constraints on the models and dust properties, resp., by allowing a direct measurement of, e.g., the distribution of direct stellar and scattered radiation. The corresponding spatial intensity distributions at $1.24 \mu\text{m}$, $1.65 \mu\text{m}$, $2.12 \mu\text{m}$, and $11 \mu\text{m}$ are shown in Fig. 5. The optical depths are $\tau(1.24 \mu\text{m}) = 5.1$, $\tau(1.65 \mu\text{m}) = 3.1$, $\tau(2.12 \mu\text{m}) = 1.9$, and $\tau(11 \mu\text{m}) = 2.2$. Although exposing an optical depth larger than unity, the inner

rim of the circumstellar shell is noticeably limb-brightened in the K' -band.

The luminosity of CIT 3 is $7791 L_{\odot}$ if $d = 500$ pc and $19945 L_{\odot}$ if $d = 800$ pc. The former value would predict CIT 3 to be an AGB star of lower mass whereas the latter indicates a more massive AGB star with a core mass larger than, say, $0.8 M_{\odot}$. Adopting a dust-to-gas ratio of 0.005 and a specific dust density of 3 g cm^{-3} , the present-day mass-loss rate can be determined to be $\dot{M} = 1.3 \cdot 10^{-5} M_{\odot}/\text{yr}$ if $d = 500$ pc and $\dot{M} = 2.1 \cdot 10^{-5} M_{\odot}/\text{yr}$ if $d = 800$ pc which is in line with the CO observations (see Sect. 1). The smaller exponent of 1.5 in the density distribution beyond $Y_2=20.5$ means that the mass-loss rate has decreased with time in the past provided the outflow velocity kept constant. Adopting $v_{\text{exp}}=20$ km/s, the kinematical age of the inner uniform outflow zone can be determined to be 87 yr.

6. Summary and conclusions

We presented the first near-infrared bispectrum speckle interferometric observations of the oxygen-rich, long-period variable AGB star CIT 3 in the J -, H -, and K' -band. The observations were taken with the Russian SAO 6m telescope. The resolution in the J -band is 88% of the diffraction-limit (48 mas), in the H -, and K' -band the resolution is fully diffraction-limited (56 mas, and 73 mas, resp.).

While CIT 3 appears almost spherically symmetric in the H - and K' -band it is clearly elongated in the J -band along a symmetry axis of position angle -28° . Two structures can be identified: a compact elliptical core and a fainter north-western fan-like structure. The eccentricity of the elliptical core, given by the ratio of minor to major axis, is approximately $\varepsilon=123 \text{ mas}/154 \text{ mas}=0.8$. The full opening angle of the fan amounts to approximately 40° , i.e. it extends from position angle -8° to -48° .

Extensive radiative transfer calculations have been carried out and confronted with the observations taking into account the spectral energy distribution ranging from $1 \mu\text{m}$ to 1 mm , our near-infrared visibility functions at $1.24 \mu\text{m}$, $1.65 \mu\text{m}$ and $2.12 \mu\text{m}$, as well as mid-infrared interferometric measurements at $11 \mu\text{m}$. It has to be noted that these calculations rely on the assumption of spherical symmetry. Given the observed elongation in the J -band, this assumption appears to be questionable at least on smaller scales. However, the main dust properties can be believed to be inferable from such models in fair approximation since the deviations from spherical symmetry appear only on smaller scales and for $\lambda < 2.1 \mu\text{m}$. Nevertheless, the derived dust-shell properties are subject to the geometry and are, therefore, of tentative character. It is due to future two-dimensional radiative transfer calculations to prove the degree of reliance of the presented models.

The best model found to match all observations refers to a cool central star with $T_{\text{eff}} = 2250 \text{ K}$ which is surrounded by an optically thick ($\tau(0.55 \mu\text{m}) = 30$) dust shell. The low temperature of the central star is constrained by the models but in particular also by the lunar occultation observations of Zappala et al. (1974) who derived a stellar diameter of 13 mas. For the given bolometric flux, this diameter can only

be achieved for low effective temperatures. The present models give a central-star diameter of $\Theta_* = 10.9$ mas being in line with these observations. Extrapolating the temperature scale of Perrin et al. (1998) based on short-period variables would predict $T_{\text{eff}} \simeq 2500\text{-}2700 \text{ K}$ for M9-10 stars. The lower effective temperature found for CIT 3 is consistent with the finding that long-period variables can be substantially cooler than giants of the same spectral type but of shorter period (van Belle et al. 1999).

The temperature at the inner rim of the dust shell amounts to $T_1 = 900 \text{ K}$. This is somewhat cooler than the usually assumed condensation temperatures for silicate grains of $1000\text{-}1200 \text{ K}$, but still well within the physical range of dust condensation temperatures and in reasonable agreement with the results of previous radiative transfer models (as e.g., $T_1 \sim 850 \text{ K}$, Le Sidaner & Le Bertre 1996; $\sim 900 \text{ K}$, Bedijn 1987 or $\sim 1000 \text{ K}$, Rowan-Robinson & Harris 1983, Lipman et al. 2000). The inner dust shell boundary is located at $r_1 = 6.6 R_*$ corresponding to an angular diameter of $\Theta_1 = 71.9 \text{ mas}$. This angular diameter is in accordance with the $2.2 \mu\text{m}$ diameter of 65 mas derived by lunar occultation observations (Zappala et al. 1974) tracing the hot dust and therefore the very inner parts of the dust shell.

Grains with various optical properties were used, the silicate grains of Ossenkopf et al. (1992) turned out to be superior to the other grain types, for instance in fitting the silicate feature. The grain sizes are strongly constrained by the near-infrared visibilities, and a grain-size distribution proved to be better suited than single-sized grains. We considered grain-size distribution according to Mathis et al. (1977), i.e. $n(a) \sim a^{-3.5}$, with $0.005 \mu\text{m} \leq a \leq a_{\text{max}}$ and determined $a_{\text{max}} = 0.25 \mu\text{m}$ as in the original MRN distribution.

Uniform outflow models, i.e. density distributions with $\rho \sim 1/r^2$, turned out to match the near- to mid-infrared part of the SED and the corresponding visibilities but to considerably underestimate the flux beyond $20 \mu\text{m}$. This indicates, for instance, either a more shallow density distribution than $\rho \sim 1/r^2$ as given by the standard uniform outflow model or the existence of regions with increased density in the outer shell due to periods of higher mass-loss in the past. The model grid was recalculated for a large variety of accordingly changed density distributions, and a two-component model existing of an inner uniform-outflow shell region ($\rho \sim 1/r^2$) and an outer region where the density declines as $\rho \sim 1/r^{1.5}$ proved to be best suited to match the observations. A $\rho \sim 1/r^{1.5}$ density distribution has also been proposed by Lipman et al. (2000) by fits of the $11 \mu\text{m}$ visibility. The present modelling suggests, however, that the flatter density fall-off should be restricted to the outer shell regions which is, for instance, constrained by the near-infrared visibilities. The transition between both density distributions takes place at $r_2 = 20.5 r_1 = 135.7 R_*$ where the dust-shell temperature has dropped to $T_2 = 163 \text{ K}$. Since these changes concern mostly the very cool regions of the shell, the other so-far discussed dust-shell properties remain basically unchanged. Provided the outflow velocity kept constant, the more shallow density distribution in the outer shell indicates that mass-loss had decreased with time in the past of CIT 3. Adopting $v_{\text{exp}} = 20 \text{ km/s}$, the termination of that

mass-loss decrease and the begin of the uniform-outflow phase took place 87 yr ago. The present-day mass-loss rate can be determined to be $\dot{M} = 1.3 \cdot 10^{-5} M_{\odot}/\text{yr}$ if $d = 500$ pc and $\dot{M} = 2.1 \cdot 10^{-5} M_{\odot}/\text{yr}$ if $d = 800$ pc being in agreement with the CO observations, and the corresponding stellar luminosity is $7791 L_{\odot}$ and $19945 L_{\odot}$, resp.

CIT 3 proved to be among the most interesting far-evolved AGB stars due to its infrared properties. Moreover, the aspherical appearance of its dust shell in the J -band puts it in one line with the few AGB stars known to expose near-infrared asphericities in their dust shells. The development of such asphericities close to the central star suggests that it is in the very end of the AGB evolution or even in transition to the proto-planetary nebula phase where most objects are observed in axisymmetric geometry (Olofsson 1996). However, in contrast to other objects, CIT 3 shows these deviations from spherical symmetry still only in the J -band, which is almost completely dominated by scattered light. This suggests that CIT 3 had just started to form aspherical structures and is in this regard still in the beginning of its very final AGB phase. If so, CIT 3 is one of the earliest representatives of this dust-shell transformation phase known so far.

Acknowledgements. The observations were made with the SAO 6 m telescope, operated by the Special Astrophysical Observatory, Russia. We thank Roger Sylvester for providing the ISO spectral energy distribution, and Rita Loidl and Bernhard Aringer for sending us their model atmospheres. The radiative-transfer calculations are based on the code DUSTY developed by Ž. Ivezić, M. Nenkova and M. Elitzur. This research has made use of the SIMBAD database, operated by CDS in Strasbourg, and of the NASA's Astrophysics Data System.

References

- Alvarez R., Lancon A., Plez B., Wood P.R., 2000, A&A 353, 322
 Aringer B., Jørgensen U.G., Langhoff S.R., 1997, A&A 323, 202
 Baud B., 1981, ApJ 250, L79
 Bedijn P.J., 1987, A&A 186, 136
 Le Bertre T., 1993, A&AS 97, 729
 Blöcker T., Balega Y., Hofmann K.-H., Weigelt G., 2001, A&A 369, 142
 Blöcker T., Balega Y., Hofmann K.-H., Lichtenthaler J., Osterbart R., Weigelt G., 1999, A&A 348, 805
 Bowers P.F., Hagen W., 1984, ApJ 285, 637
 Bowers P.F., Johnston K.J., Spencer J.H., 1983, ApJ 274, 733
 David P., Pegourie B., 1995, A&A 293, 833
 Desmurs J.F., Bujarrabal, Colomer F., Alcolea J., 2000, A&A 360, 189
 Dickinson D.F., 1976, ApJS 30, 259
 Dickinson D.F., Reid M.J., Morris M., Redman R., 1978, ApJ 220, L113
 Draine B.T., Lee H.M., 1984, ApJ 285, 89
 Dyck H.M., Lockwood G.W., Capps R.W., 1974, ApJ 189, 89
 Dyck H.M., van Belle G.T., Thompson R.R., 1998, AJ 116, 981
 Dyck H.M., Benson J.A., van Belle G.T., Ridgway S.T., 1996, AJ 111, 1705
 Epchtein N., Guibert J., Nguyen-Quang-Rieu, Turon P., Wamsteker W., 1980, A&A 85, L1
 Fouque P., Le Bertre T., Epchtein N., Guglielmo F., Kerschbaum F., 1992, A&AS 93, 151
 Gauger A., Balega Y., Irrgang P., Osterbart R., Weigelt G., 1999, A&A 346, 509
 Jones T.J., Bryja C.O., Gehrz R.D., Harrision T.E., Johnson J.J., Klebe D.I., Lawrence G.F., 1990, ApJS 74, 785
 Harvey P.M., Bechis K.P., Wilson W.J., Ball J.A., 1974, ApJS 248, 331
 Herman J., Habing H.J., 1985, A&AS 59, 523
 Hofmann K.-H., Weigelt G., 1986, A&A 167, L15
 Hyland A.R., Becklin E.E., Frogel J.A., Neugebauer G., 1972, A&A 16, 204
 IRAS, Point Source Catalogue, 1985, US Government Publication Office
 Ivezić Ž., Elitzur M., 1997, MNRAS 287, 799
 Ivezić Ž., Nenkova M., Elitzur M., 1997, User Manual for DUSTY, University of Kentucky (<http://www.pa.uky.edu/moshe/dusty>)
 Jewell P.R., Webber J.C., Snyder L.E., 1980, ApJ 242, L29
 Knapp G.R., Morris M., 1985, ApJ 292, 640.
 Knapp G.R., Philips T.G., Leighton R.B., Lo K.Y., Wannier, P.G., Wootten H.A., Huggins P.J., 1982, ApJ 252, 616.
 Kruszewski A., Coyne G.V., 1976, AJ 81, 641
 Labeyrie A., 1970, A&A 6, 85
 Lambert D.L., Hinkle K.H., Smith V., 1990, AJ 99, 1612
 Lancon A., Wood P.R., 2000, A&AS 146, 217
 Lipman E.A., Hale D.D., Monnier J.D., Tuthill P.G., Dnachi W.C., Townes C.H., 2000, ApJ 532, 467
 Lockwood G.W., 1985, ApJS 58, 167
 Lohmann A.W., Weigelt G., Wirtitzer B., 1983, Appl. Opt. 22, 4028
 Loup C., Forveille T., Omont A., Paul J.F., 1993, A&AS 99, 291.
 Markwick A.J., Millar T.J., 2000, A&A 359, 1162
 Marengo M., Busso M., Silvestro G., Persi P., Lagage P.O., 1999, A&A 348, 501
 Mathis J.S., Rimpl W., Nordsieck K.H., 1977, ApJ 217, 425 (MRN)
 Matsuura M., Yamamura I., Murakami H., Onaka T., 2001, in: Post-AGB Objects as a Phase of Stellar Evolution, R. Szczerba and S. K. Gorny (ed.), ASSL 265, Kluwer, Dordrecht, p. 433.
 McCall A., Hough J.H., 1980, A&AS 42, 141
 McCarthy D.W., Low F.J., Howell R., ApJ 214, L85
 Merrill K.M., Stein W.A., 1976, PASP 88, 294
 Monnier J.D., Geballe T.R., Danchi W.C., 1998, ApJ 502, 833
 Morrison D., Simon T., 1973, ApJ 186, 193
 Neri R., Kahane C., Lucas R., Bujarrabal V., Loup C., 1998, A&AS 130, 1
 Neugebauer G., Leighton R.B., 1969, Two Micron Sky Survey, NASA SP-3047
 Olofsson H., 1996, ApSS 245, 169
 Olmon F.M., Winnberg A., Matthews H.E., Schultz G.V., 1980, A&AS 42, 119
 Ossenkopf V., Henning T., Mathis J.S., 1992, A&A 261, 567
 Perrin G., Coude du Foresto V., Ridgway S.T., Mariotti J.M., Traub W.A., Carleton N.P., Lacasse M.G., 1998, A&A 331, 619
 Price S.D., Murdock T.L., 1983, The Revised Air Force Geographical Laboratory (RAFGL) Infrared Sky Survey Catalog, AFGL-TR-83-0161
 Rowan-Robinson M., Harris S., 1983, MNRAS 202, 767
 Schutte W.A., Tielens A.G.G.M., 1989, ApJ 343, 369
 Le Sidaner P., Le Bertre T., 1993, A&A 278, 167
 Le Sidaner P., Le Bertre T., 1996, A&A 314, 896
 Sopka R.J., Hildebrand R., Jaffe D.T., Gatley I., Roelig T., Werner M., Jura M., Zuckerman B., 1985, ApJ 294, 242
 Sopka R.J., Olofsson H., Johansson L.E.B., Nguyen-Q-Rieu, Zuckerman B., 1989, A&A 210, 78.
 Strecker D.W., Ney E.P., 1974, AJ 79, 1410
 Sudol J.J., Dyck H.M., Stencel R.E., Klebe D.I., Creech-Eakman M.J., 1999, AJ 117, 1609
 Suh K.W., Jones T.J., 1997, ApJ 479, 918

- Sylvester R.J., Kemper F., Barlow M.J., de Jong T., Waters L.B.F.M., Tielens A.G.G.M., Omont A., 1999, *A&A* 352, 587
- Ulrich B.T., Neugebauer G., McCammon D., Leighton R.B., Hughes E.E., Becklin E., 1966, *ApJ* 146, 288
- van Belle G.T., Dyck H.M., Benson J.A., Lacasse M.G., 1999a, *AJ* 112, 2147
- van Belle G.T., Lane B.F., Thompson R.R. et al., 1999b, *AJ* 117, 521
- van Herk G., 1965, *Bull. Astron. Inst. Netherlands* 18, 71
- van Langevelde H.J., van der Heiden R., van Schooneveld C., 1990, *A&A* 239, 193
- Volk K., Cohen M., 1989, *AJ* 98, 931
- Walmsley C.M., Chini R., Kreysa E., Steppe H., Forveille T., Omont A., 1991, *A&A* 248, 555
- Weigelt G., 1977, *Optics Commun.* 21, 55
- Wilson W.J., Barrett A.H., Moran J.M., 1970, *ApJ* 160, 545
- Wisniewski W.Z., Wing R.F., Spinrad H., Johnson H.L., 1967, *ApJ* 148, L29
- Whitelock P., Menzies J., Feast M., Marang F., Carter B., Roberts G., Catchpole R., Chapman J., *MNRAS* 267, 711
- Xiong G.Z., Chen P.S., Gao H., 1994, *A&AS* 108, 661
- Zappala R.R., Becklin E.E., Matthews K., Neugebauer G., 1974, *ApJ* 192, 109

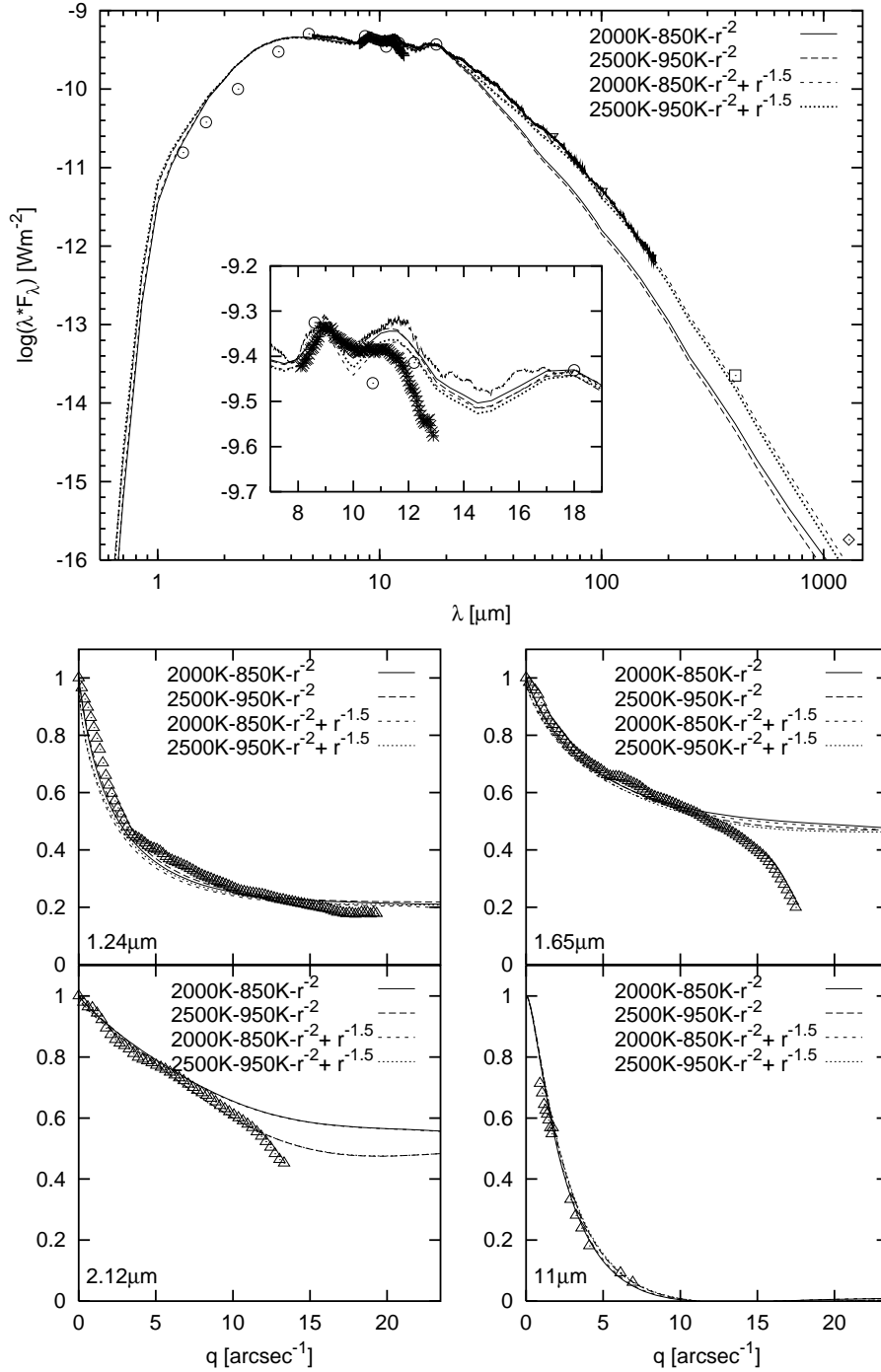


Fig. 3. Model SED and visibilities at 1.24 μm, 1.65 μm, 2.12 μm, and 11 μm for models with $(T_{\text{eff}}, T_1) = (2000 \text{ K}, 850 \text{ K})$ and $(2500 \text{ K}, 950 \text{ K})$, resp. Both uniform outflow models ($\rho \sim 1/r^2$; solid and long-dashed lines) and models with a flatter density distribution in the outer shell region ($\rho \sim 1/r^2$ for $Y \leq 20.5$ and $\rho \sim 1/r^{1.5}$ for $Y > 20.5$; short-dashed and dotted lines) are shown. The optical depth $\tau_{0.55 \mu\text{m}}$ is 30. The calculations are based on a black body, Ossenkopf et al. (1992) silicates, and an MRN grain size distribution with $a_{\text{max}} = 0.25 \mu\text{m}$. The symbols refer to the observations. SED — \circ : Jones et al. (1990) [$\phi = 0.77$]; \square : Sopka et al. (1985) [$\phi = 0.89$]; \diamond : Walmsley et al. (1991) [$\phi = 0.73$]; ∇ : IRAS fluxes (scaled to ISO data); $*$: spectrophotometry of Monnier et al. (1998) [interpolated for $\phi = 0.75$]; thick line: ISO spectroscopy of Sylvester et al. (1999) [adjusted to match the Jones et al. (1990) photometry at 9 μm and 18 μm]. The inlay shows the Jones et al. (1990) and Monnier et al. (1998) data together with the ISO spectroscopy of Sylvester et al. (1999). Near-infrared visibilities — \triangle : present speckle observations. Mid-infrared visibility — \triangle : ISI observations at 4m, 9.6m and 16m baseline of Lipman et al. (2000).